

A DCE-MRI Driven 3-D Reaction-Diffusion Model of Solid Tumour Growth

Thaís Roque¹, Laurent Risser², Veerle Kersemans³, Sean Smart³, Danny Allen³, Paul Kinchesh³, Stuart Gilchrist³, Ana L. Gomes³, Julia A. Schnabel^{1,4}, *Member, IEEE*, Michael A. Chappell¹

Abstract—Predicting tumour growth and its response to therapy remains a major challenge in cancer research and strongly relies on tumour growth models. In this work, we introduce, calibrate and verify a novel image-driven reaction-diffusion model of avascular tumour growth. The model allows for proliferation, death and spread of tumour cells, and accounts for nutrient distribution and hypoxia. It is constrained by longitudinal time series of DCE-MRI images. Tumour specific parameters are estimated from two early time points and used to predict the spatio-temporal evolution of the tumour volume and cell densities at later time points. We first test our parameter estimation approach on synthetic data from 15 generated tumours. Our *in silico* study resulted in small volume errors ($< 5\%$) and high Dice overlaps ($> 97\%$), showing that model parameters can be successfully recovered and used to accurately predict tumour growth. Encouraged by these results, we apply our model to seven pre-clinical cases of breast carcinoma. We are able to show promising preliminary results, especially for the estimation for early time points. Processes like angiogenesis and apoptosis should be included to further improve predictions for later time points.

Index Terms—Animal models and imaging, Magnetic resonance imaging (MRI), Quantification and estimation, Tissue modelling

I. INTRODUCTION

CANCER is a leading cause of death worldwide. It can be seen as a progressive multistep transformation process that incorporates biological changes happening at different spatial and temporal scales. Mathematical models of tumour growth provide a framework within which this biological system can be analysed. Broadly speaking, mathematical models can be classified into two categories depending on the scale the focus resides on: microscopic and macroscopic models.

The first category describes the evolution of each tumour cell by different biological functions and activities to elucidate the microscopic aspect of tumour growth. Models can range from simple exponential, logistic and Gompertzian growth

laws to elaborate systems of partial differential equations describing the growth of a tumour and its invasion into the surrounding tissue [5], [8], [18], [22].

Although these models can provide helpful insights into tumour biology, their clinical usefulness is fundamentally limited. This is because the majority of these models rely on knowledge of processes occurring at the sub-cellular or cellular scales, such as chemotaxis, haptotaxis or growth factors, which are difficult or even impossible to measure in an intact living system and cannot be observed in medical images.

The second category includes continuum models that describe tumour growth at the macroscopic level. The majority of the current macroscopic models of tumour growth have been applied to the case of glioma growth [7], [11]–[13], [15], [24], [25], [28]. Formulated based on Murray’s reaction-diffusion formalism [17], they describe the temporal evolution of tumour cell densities at different locations through diffusion, migration and proliferation of cells.

By describing the evolution of cell groups rather than of each individual cell, these models provide a framework which allows for integration of medical imaging data. In order to personalise such a model, the estimation of parameters using longitudinal data can be performed to predict subsequent evolution. Here, evolution can be defined as cellular, volumetric, or tumour delineation progression. Most groups initialise their models with cellular densities but use a macroscopic, observable quantity of interest (e.g. radial or middle slice evolution) for validation [7], [11], [13], [24], [28]. Following the idea that in the images only the evolution of tumour boundaries but not the tumour cell densities can be observed, other studies have chosen to parametrise their models by following the motion of the tumour delineation [15].

Independent of whether their parametrisation is based on cellular density evolution or on tumour delineation progression, all of the above macroscopic models focus on the integration of anatomical medical imaging. Although some studies have included structural information from Diffusion Tensor Imaging (DTI) to model the fact that glioma cells preferentially migrate along white fibres of the brain, no information on the metabolic and activity status of the cell densities was included [7], [13].

Some studies have integrated metabolic measures from medical imaging modalities into a model of tumour growth. This was done, for example, by linking the biological aggressiveness assessed by a series of MRI with the hypoxic burden assessed on FMISO-PET [26]; by using PET-MRI data to constrain a coupled set of partial differential equations to

¹ Institute of Biomedical Engineering, Dept. of Engineering Science, University of Oxford, UK

² CNRS, Institut de Mathématiques de Toulouse, France

³ CRUK/MRC Oxford Institute for Radiation Oncology, Department of Oncology, University of Oxford, UK

⁴ Division of Imaging Sciences and Biomedical Engineering, King’s College London, UK

Corresponding author’s email: michael.chappell@eng.ox.ac.uk

All data underpinning the results of this paper can be accessed under: <https://ora.ox.ac.uk/objects/uuid:e01908c5-5299-407b-ba60-acc4af3f0353>

Copyright (c) 2017 IEEE. Personal use of this material is permitted. However, permission to use this material for any other purposes must be obtained from the IEEE by sending a request to pubs-permissions@ieee.org.

describe tumour cell proliferation, angiogenesis, and glucose consumption [32]; by using hypoxia as a driver of tumour cell migration described in terms of imaging data (MRI, PET and SPECT) [4]; or by using Diffusion Weighted MRI and Dynamic Contrast-Enhancement (DCE)-MRI to parametrise a logistic model of tumour model and predict the cellular evolution as well as the reaction of tumour to therapy [3].

All of these studies were able to demonstrate the feasibility of parametrising a model of tumour growth using information from imaging data. However, due to the lack of subject-specific data, especially in face of the multi-modality approach, a mix of parameters from various studies using different types of cancer needed to be used.

To circumvent the problem of multi-modality and hence the potential lack of subject-specific data, in this work, we derived all information needed to drive a model of tumour growth from a single imaging modality. This modality needs to be able to provide anatomic information (ideally 3D) whilst allowing for richer information on microscopic phenomena to be extracted. Dynamic Contrast-Enhancement (DCE)-MRI, which additionally to the anatomic MRI information enables the extraction of physiological parameters related to vessel permeability, blood flow, and tissue volume fractions was chosen [27]. It has previously been shown that DCE-MRI has the potential to predict therapeutic response at the cellular level [29] and to assess tumour patophysiology by estimation of tumour cellularity [2], [3].

The contributions of this work are threefold: 1. We design a subject-specific preclinical tumour growth model that allows for the inclusion of anatomical information as well as of different biological activities (proliferation, hypoxia and necrosis) extracted from DCE-MRI data; 2. We extend our previous discrete model [21] used to simulate the 2-D expansion of the middle slice of the tumour to a 3-D reaction-diffusion model able to simulate the expansion of tumour volume; 3. We test our model first on synthetic data to derive the means to accurately recover model parameters and then on cases of preclinical breast carcinoma to predict the local cell density for each cell sub-population (proliferative, hypoxic and necrotic), as well as the 3-D macroscopic invasion of the tumour in the host tissue at later time points.

II. METHODS

A. Overview of the Method

Due to its capacity to characterize tumour tissue properties at the macroscopic and microvascular scales, we use DCE-MRI time series to build, calibrate and validate our PDE model and simulate the spatio-temporal evolution of tumours.

The general pipeline is summarized in Fig. 1. Firstly, local physiological properties of the same tumour at two consecutive time points $TP1$ and $TP2$ are extracted from the DCE-MRI time series (section II-C) and then converted into cellularity maps (section II-D). The tumour evolution between the time points is assumed to follow the PDE model outlined in section II-B. To make this model tumour-specific, parameters are calibrated by maximizing the similarity between the transformed cellularity maps of $TP1$ and the observed cellu-

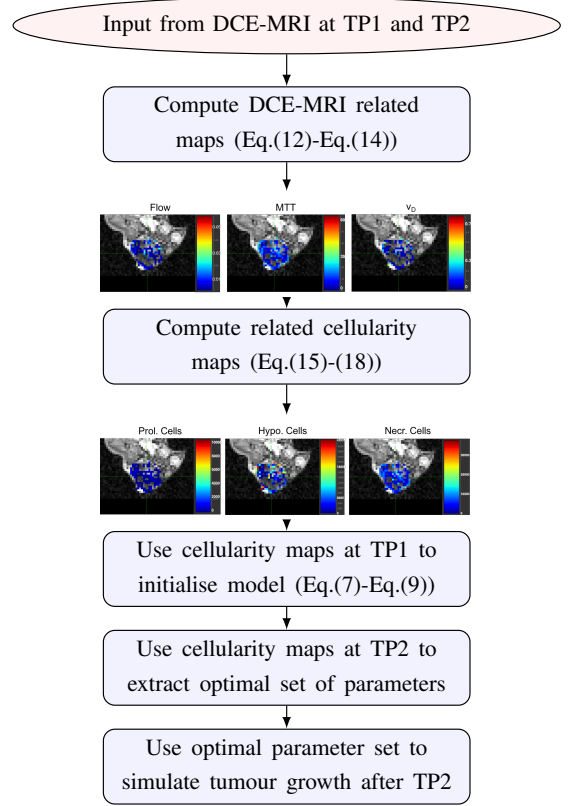


Fig. 1: Overview of a tumour growth model built from DCE-MRI perfusion imaging data. DCE-MRI related physiological maps are used to compute proliferating, hypoxic and necrotic cell maps used to initialise the model expressed as a set of partial-differential equations. This model is solved at each time step and voxel, to compute the cellularity maps and tumour volume at a later TP. The true tumour volume at $TP2$ is used to optimise a set of parameters, which is in turn used to predict the tumour at a later TP.

larity maps at $TP2$ using a simulated annealing optimisation technique (section II-E). The PDE model of section II-B is finally used to predict the tumour development after $TP2$ (section II-F) and compared to the tumours observed in the scans of these time points (section III).

B. Tumour growth model

The tumour growth model presented in this work represents a multiscale 3-D model consisting of three layers: a macroscopic tissue layer to allow for integration of the pre-clinical imaging data, a cellular layer at which the nutrient is made available to the tumour cells and a sub-cellular layer in which metabolic processes depending on the nutrient level can lead to cell proliferation, hypoxia or necrosis. Changes in the latter (i.e. mitotic activity, hypoxia and necrosis) result in changes in the microscopic layer (i.e. local cell number), which in turn affect the tumour at the macroscopic level (i.e. tumour expansion and nutrient distribution).

Proliferation has been investigated in various mathematical models. The most prominent models are given by the logistic and Gompertz models. Due to its simplicity when compared to the Gompertz law, the logistic law has been implemented to our model of tumour growth in the form:

$$\frac{\partial c(t)}{\partial t} = g(c(t)), \quad (1)$$

where $c(t)$ is the cell number and $g(c(t))$ is:

$$g(c(t)) = p \cdot c(t) \cdot \left(1 - \frac{c(t)}{\Theta}\right), \quad (2)$$

where Θ the carrying capacity of the voxel obtained by dividing the voxel volume (here 0.0751mm^3) by the volume of each cell, which is assumed to be a sphere with a diameter of 10μ as given in [3], and p the rate at which cells proliferate. The solution for this model depicts an S-shape curve. This means that as time t increases, the cell number $c(t)$ increases first slowly then more rapidly as the graph approaches a straight line in the midsection, followed by a slow increase until finally a saturation state is reached.

As time increases, tumour cells not only proliferate, but also spatially invade the hosting tissue. To implement spatial diffusion into pure, temporal proliferating models, Eq. (1) needs to be extended by the spatial tumour expansion term. Hence, Eq. (1) for the logistic model becomes a reaction-diffusion equation as follows:

$$\frac{\partial c(\mathbf{x}, t)}{\partial t} = \nabla \cdot (d(\mathbf{x}, t) \nabla c(\mathbf{x}, t)) + p \cdot c(\mathbf{x}, t) \cdot \left(1 - \frac{c(\mathbf{x}, t)}{\Theta}\right), \quad (3)$$

where the carrying capacity of each voxel Θ is introduced to model the saturation of nutrient.

Because tumour growth is not only the result of unrestrained proliferation, but also of disorder in cell death and hypoxia, our model includes the evolution of proliferating, hypoxic and necrotic cells.

At each time step t , proliferating cells can either divide following a Gompertz curve, or if their nutrient level is low, become hypoxic following an exponential decay. In turn, hypoxic cells can either remain hypoxic or die following an exponential decay. The maps for the cell division probability g , the hypoxia transition f and the necrosis transition h are directly related to the nutrient map η , as follows:

$$g(\eta(\mathbf{x}, t)) = c_{g0} \exp(-\exp(-c_g \cdot (\eta(\mathbf{x}, t) - ip))) \quad (4)$$

$$f(\eta(\mathbf{x}, t)) = \exp(-c_f \cdot \eta(\mathbf{x}, t)) \quad (5)$$

$$h(\eta(\mathbf{x}, t)) = \exp(-c_h \cdot \eta(\mathbf{x}, t)). \quad (6)$$

where c_{g0} , c_f and c_h are model parameters. The constant c_g represents the slope of the Gompertz function and is set to $c_g = 0.31/\text{mmHg}$ to reach 99% of the asymptote c_{g0} at maximal nutrient availability; and ip is the position of the steepest increase of the nutrient, and therefore the inflection point of the Gompertz curve. To reduce the number of parameters, we set $c_h = 2c_f$, accounting for the fact that the transition between hypoxia and necrosis happens at a lower nutrient level than the one between proliferation and hypoxia, and assume $ip = 15\text{mmHg}$ for all cases.

Expressed as a set of PDEs, the processes described above can be modelled as follows [22]:

$$\begin{aligned} \frac{\partial p(\mathbf{x}, t)}{\partial t} = & \nabla \cdot (d(\mathbf{x}, t) \nabla p(\mathbf{x}, t)) + g(\eta(\mathbf{x}, t)) \cdot p(\mathbf{x}, t) \\ & \cdot \left(1 - \frac{r(\mathbf{x}, t)}{\Theta}\right) - f(\eta(\mathbf{x}, t)) \cdot p(\mathbf{x}, t) \end{aligned} \quad (7)$$

$$\begin{aligned} \frac{\partial q(\mathbf{x}, t)}{\partial t} = & \nabla \cdot (d(\mathbf{x}, t) \nabla q(\mathbf{x}, t)) + f(\eta(\mathbf{x}, t)) \cdot p(\mathbf{x}, t) \\ & - h(\eta(\mathbf{x}, t)) \cdot q(\mathbf{x}, t) \end{aligned} \quad (8)$$

$$\frac{\partial n(\mathbf{x}, t)}{\partial t} = h(\eta(\mathbf{x}, t)) \cdot q(\mathbf{x}, t) \quad (9)$$

where $p(\mathbf{x}, t)$, $q(\mathbf{x}, t)$, $n(\mathbf{x}, t)$ and $r(\mathbf{x}, t)$ represent the number of proliferative, quiescent (hypoxic), necrotic and total cells, with t denoting time and \mathbf{x} a spatial coordinate in a three-dimensional domain. Note that, other than in Eq. (3) and in most reaction-diffusion models of tumour growth [3], [7], [11], [13], [15], [24], [26], [28] where the proliferation rate had a global value, in our work the proliferation rate, $g(\eta(\mathbf{x}, t))$, is a function of the nutrient distribution (Eq. 4) and hence, of time and space¹. Once necrotic, cells are removed from the tumour after a period of 40 hours, modelling the lysis time [8].

Once necrotic, cells are removed from the tumour after a period of 40 hours, modelling the lysis time [8].

C. DCE-MRI data to physiological parameters

Dynamic Contrast Enhancement (DCE) MR perfusion imaging is based on the application of an exogeneous, intravascular, non-diffusible contrast agent (CA) and consists of taking several sequential T1-weighted MR images over a short period of time upon the injection of a CA. The most common CA used is the low-molecular-weight gadolinium-diethylenetriamine pentaacetic acid (Gd-DTPA), which is able to transverse the vessel walls, thus entering the extracellular-extravascular space (EES). However, it is unable to cross the cellular membrane, limiting its volume of distribution (v_D) to the interstitial space. As a result, DCE-MRI signal intensity changes derive mainly from CA that extravasates to the EES, which locally enhances the measured signal intensities by shortening of the longitudinal relaxation time according to its concentration $C(t)$:

$$\frac{1}{T_1} = \frac{1}{T_{10}} + r_1 C(t) \quad (10)$$

Here, T_{10} is the relaxation time T_1 prior to the injection of CA, r_1 the relaxivity constant specific to CA, and $C(t)$ the total concentration of CA at time t .

A usual DCE-MRI experiment assumes a tissue sample with a single inlet through which the arterial plasma flow F enters the tissue. The measured time curves, the tissue concentration $C(t)$ and the concentration in the blood plasma of the feeding artery (the arterial input function, AIF), are related by convolution with an unknown, tissue-characteristic impulse response function $I(t)$:

$$C(t) = I(t) \otimes AIF \quad (11)$$

¹The numerical strategy used to solve the system of equations, in particular Equations (7), (8) and (9), is developed in Appendix-A, which can be found in the supplementary materials available in the supplementary files/multimedia tab.

Several models have been developed to estimate DCE-MRI related parameters. The first generation dates back to the works of Tofts and colleagues in the 1990s [27]. Here, perfusion related parameters (e.g. exchange rates between individual subspaces) are obtained by fitting a Pharmacokinetic Tracer Analysis model to $C(t)$. Model-free approaches that characterize the shape and structure of the signal intensity time curve $S(t)$ can also be used to quantify tissue perfusion [35]. Further, semi-quantitative parameters (e.g. bolus arrival time, area under the curve and time to peak) can be computed directly from the $S(t)$ [20].

For our strategy we are interested in the following physiological quantities from the DCE-MRI time series obtained at each time point:

- The maximum enhancement peak of the concentration time curve (mEP),
- the distribution volume (v_D) defined as the fraction of tissue accessible to the CA,
- the blood flow (F),
- the Mean Transit Time (MTT) which relates v_D to the arterial inlet to the space carrying the plasma flow.

To extract these parameters, we adopt a combination of the model-free deconvolution method with a semi-quantitative approach. Note that in this subsection, t indexes the images of a single DCE-MRI time sequence and not different time points TPn , so that it is much smaller here than in section II-B.

First, $S(t)$ is converted into CA concentration time curve $C(t)$ using:

$$C(t) = \frac{1}{r_1} \left(\frac{-1}{TR} \ln \left\{ \frac{E(E_{10}-1)+E_{10}[1-\cos(FA)]}{1+\cos(FA)[E(E_{10}-1)-1]} \right\} - \frac{1}{T_{10}} \right)$$

where $E_{10} = \exp(-TR/T_{10})$, $E = S(t)/S_0$ and r_1 is the longitudinal relaxivity (contrast agent property). TR is the repetition time (time between two excitation pulses), FA denotes the flip angle and S_0 is the signal at the baseline. It follows that the $C(t)$ can be extracted from the observed signal enhancement E , provided that r_1 , T_{10} and TR are known. The maximum enhancement peak of the concentration time curve mEP is then defined as equal to $\max_t(C(t))$.

Next, the distribution volume v_D (the fraction of tissue accessible to the CA) map for each TP can be computed using Eq. (12) as given in [23]:

$$v_D = \frac{\int_0^\infty C(t)dt}{\int_0^\infty AIF(t)dt} \quad (12)$$

A population based AIF as given in [19], using pre-clinical values as in [10], was used.

Following Eq. (11), the deconvolution of the measured $C(t)$ with AIF yields an estimate for the impulse function $I(t)$, defined as:

$$I(t) = F \cdot R(t) \quad (13)$$

Here, $R(t)$ represents the residue function, the fraction of CA remaining in the voxel at a time t after its arrival. For the deconvolution, a block-circulant singular value decomposition (oSVD) matrix as described in [31] was used. Applying oSVD

to Eq. (11) and (13), yields the blood flow F as the maximum of $I(t)$.

The MTT for each voxel can be computed using the central-volume theorem [34]:

$$MTT = \frac{v_D}{F} \quad (14)$$

All these parameters quantify the tumour metabolic status, which is important for the tumour further development.

D. Cellularity maps and related maps

Different maps are needed to initialise, calibrate and verify our reaction-diffusion model: The number of proliferating cells (p), the number of hypoxic cells (q), the number of necrotic cells (n), the total number of tumour cells (r), the nutrient distribution (η) and the diffusion coefficient of the hypoxic and proliferative cell densities (d).

Aryal *et al.* were able to demonstrate that DCE-MRI derived v_D values were significantly, negatively correlated with tumour cellularity [2]. Building on these findings, to estimate the total number of tumour cells r at a given voxel location \mathbf{x} , we assume that the higher v_D the less space for cells within a voxel. We also assume that the higher the cellularity, the longer it will take for the CA to leave the voxel. Hence, a positive correlation between cellularity and MTT is assumed:

$$r(\mathbf{x}) = \left(\frac{MTT(\mathbf{x})}{\max(MTT(\mathbf{x}))} \right) \cdot (1 - v_D(\mathbf{x})) \cdot \Theta \quad (15)$$

The number of proliferating cells p is assumed to be proportional to the peak of maximum enhancement mEP , based on findings in [9] who were able to demonstrate a positive correlation between the mitotic index and the peak of maximum enhancement. It follows that an initial map giving the number of proliferating cells can be estimated assuming the following relationship:

$$p(\mathbf{x}) = \frac{mEP(\mathbf{x})}{\max(mEP(\mathbf{x}))} \cdot r(\mathbf{x}). \quad (16)$$

Cells within a voxel that are not proliferating can either be in a dormant state (hypoxic) or dead (necrotic). In order to obtain the number of necrotic cells n , we assume that low blood flow F , and hence low nutrient availability, results in high cell death rate calculated as follows:

$$n(\mathbf{x}) = \left(1 - \frac{F(\mathbf{x})}{\max(F(\mathbf{x}))} \right) \cdot (r(\mathbf{x}) - p(\mathbf{x})). \quad (17)$$

Finally, the number of hypoxic cells q can be estimated as the difference between the total cell number $r(\mathbf{x})$ and the sum of $p(\mathbf{x})$ and $n(\mathbf{x})$:

$$q(\mathbf{x}) = r(\mathbf{x}) - p(\mathbf{x}) - n(\mathbf{x}). \quad (18)$$

Once the total number of cells in each voxel is known, the nutrient distribution $\eta(\mathbf{x})$ is computed using:

$$\eta(\mathbf{x}) = \eta_0 \cdot [(1 - \alpha \cdot r(\mathbf{x})) / [1 + (p(\mathbf{x})/\gamma)]] \quad (19)$$

Here, η_0 is assumed to be the level of nutrient of the host tissue (in the absence of a tumour cell population) which is equal to the maximum of the nutrient that can be made

Time point	Case 1	Case 2	Case 3	Case 4	Case 5	Case 6	Case 10
$c_f[1/mmHg]$	0.063	0.112	0.072	0.290	0.100	0.1316	0.082
$D_0[mm^2/h]$	1.59E-07	2.46E-05	5.5E-05	1.89E-05	5.0E-06	1.82E-05	3.42E-07

TABLE I: Optimized model parameter values used to simulate tumour growth between $TP2$ and $TP5$. c_{g_0} was kept fixed at $0.0001 [1/h]$ for all synthetic and pre-clinical cases.

available for cells within the tumour. The constants α and γ are chosen, for simplicity, to be the inverse of the maximum of the total cell number r and of the proliferative cell number p , respectively. This is the quasi-steady state solution to

$$\frac{\partial \eta(\mathbf{x})}{\partial t} = D_\eta \nabla \eta(\mathbf{x}) + k_1 \cdot n_0(1 - \alpha \cdot (r(\mathbf{x}))) - k_1 \cdot c - k_2 \cdot p(\mathbf{x}) \cdot \eta(\mathbf{x}), \quad (20)$$

where $\gamma = k_1/k_2$. This quasi-steady state assumption can be justified by the disparity in time-scale between the dynamics of the nutrient field and the movement of the interface (the diffusion time of oxygen across one cell is on the order of seconds while cell division occurs on the order of hours). The first term of the right-hand side can be set to zero, as the nutrient can be assumed to be consumed locally by cells within this voxel and not by cells in neighbouring voxels.

We finally assume the isotropic diffusion coefficient d of both the hypoxic q and proliferative p cell densities to be related to the total cell number r as follows:

$$d(\mathbf{x}, t) = D_0 \exp(-r(\mathbf{x}, t)/\kappa) \quad (21)$$

κ is chosen to be the maximum of the total cell number, *i.e.* $1/\alpha$, and D_0 is a parameter to be optimised to model the fact that tumours expand at different rates.

E. Estimation of tumour-specific parameters

Parameter maps derived from DCE-MR images at $TP1$ are used to initialise the model. In order to predict the tumour evolution after $TP2$ using the model of section II-B, the parameters c_{g_0} , c_f and D_0 have to be estimated.

Our estimation problem can be defined as:

$$\begin{aligned} \min_{c_{g_0}, c_f, D_0} \quad & vol_e(c_{g_0}, c_f, D_0) \\ \text{s.t.} \quad & 0.0001 \leq c_{g_0} \leq 0.01 \quad 1/h \\ & 0.05 \leq c_f \leq 0.3 \quad mmHg/h \\ & 1 \times 10^{-7} \leq D_0 \leq 0.01 \quad mm^2/h \end{aligned} \quad (22)$$

where $vol_e = |(vol_s - vol_t)/vol_t|$ is the relative volume estimation error between the volume observed at the true scans in $TP2$ which have been manually delineated by a radiologist (vol_t), and the simulated volume, vol_s , obtained by producing an apparent boundary on the simulated tumour based on $r(x, TP2)$. The cellularity maps are simulated solving the set of PDEs (Eq. 7-Eq. 9). Their initial states are computed at $TP1$ using the methods described in II-C and II-D. Due to the diffusion term, all voxels of $r(x, TP2)$ might contain some tumour cells even if they would not be visible on a scan. In order to delineate the simulated tumour, we assume a voxel x to be outside the tumour if less than 1% of its carrying capacity is made out of tumour cells, *i.e.* if $r(x, TP2) < 0.01\Theta$. Note

that this PDE-constrained optimisation problem is nonconvex and computing vol_e gradients would be costly. We then use a global optimisation strategy, the built-in simulated annealing MATLAB function [14], to optimise Eq. 22 and hence estimate c_{g_0} , c_f and D_0 .

F. Predicting the tumour spatio-temporal growth

Once the parameters c_g , c_f and D_0 are estimated between time points $TP1$ and $TP2$, the obtained values after optimisation (see Tab. I) are used as input for the tumour growth simulation between $TP1$ and $TP5$. After simulation, the output, represented by the simulated cellularity maps and the simulated tumour volume, was compared to the maps acquired at the respective time points.

We also compare the simulated tumour volumes with the true volumes observed in the actual scans in terms of the Dice similarity coefficient DSC . This statistical validation metric, normally used to evaluate the performance of segmentation tools in terms of spatial overlap accuracy, can be calculated using $DSC = \frac{2A \cap B}{A+B}$, where A is the simulated tumour image and B the true tumour image at a given TP .

The calibration process takes on average 14.84 ± 4.79 hours and around 1500 iterations over the 3D growth simulation between $TP1$ and $TP2$ until convergence is achieved. For the prediction post $TP2$, each run takes up to 3 minutes depending on the size of the tumour being modelled. All codes were written in Matlab (Mathworks, Natick, MA) and all simulations performed on a 3.4 GHz Intel Xeon machine with 32GB of RAM, providing scope for reducing the optimisation time using more efficient implementations or parallelization.

G. Experiments

1) *Sensitivity analysis:* To explore whether all of our parameters influence our model outcome, we performed a sensitivity analysis using the eFAST method as described in [16]. The reference outputs were $r(\mathbf{x})$ and vol_s . To determine the significance of the eFAST first-order indexes we followed the procedure described in [16] and included a dummy parameter into the analysis. Parameters with a sensitivity index with less than that of the dummy parameter should be considered not significantly different from zero.

2) *Synthetic data:* In order to evaluate our parameter estimation method, we performed tests with 15 different synthetic tumours generated using 15 different parameter sets within the ranges given in Eq. 22. For each tumour the model is initialised using maps for $TP1$ from one of the available pre-clinical DCE-MRI extracted following section II-D and simulations were performed for four days, *i.e.* up to $TP5$. We note that no noise has been added to the simulation since the relationship

between MR signal noise and the noise seen in our input (cellularity maps) is not known and its analysis would exceed the scope of the current study.

3) *Pre-clinical data*: Ten mice, in which CaNT (breast carcinoma) tumour cells were injected, were imaged at five consecutive days over the tumour growth cycle (starting 10 days after injection). We denote TPn the time point of the n th acquisition. DCE-MRI was performed at 4.7 T (Varian VN-MRS) with 60 repeats (DCE frame rate of 10-15 seconds) of a cardio-respiratory (CR-) gated RF and gradient spoiled 3-D gradient echo scan (TR1.4 ms, TE=0.64 ms, FOV=54×27×27 mm³, matrix=128×64×64, hard pulse=16 μs and FA=5°). Anaesthesia was maintained with 1-3% isoflurane in a 1:5 O₂:air mixture. Respiration was monitored using a pressure balloon. ECG needles were placed subcutaneously in the chest. Motion artefact was minimised with automatic and immediate reacquisition of data corrupted by respiration motion. Gd3+ was automatically infused into the lateral tail vein triggered at the start of scan 11/60. Sporadically, the Gadolinium injection failed, which hindered the acquisition of the DCE-MRI for $TP1$ for Case 3, $TP2$ for Cases 8 and 9, $TP3$ for Case 1, $TP4$ for Case 9 and $TP5$ for Cases 3 and 4. T10 was determined prior to DCE-MRI from a variable flip angle (VFA) scan [6] with the same CR-gated 3-D gradient echo scan and 16 nominal FAs ranging from 1° to 7° in steps of 0.4°. 3-D B1 maps to quantify FA prescription were acquired with a respiration gated actual flip angle imaging (AFI) scan [33] and TR1=10 ms, TR2=100 ms, TE=0.42 ms and nominal FA=64°. Due to missing information for $TP2$ Cases 8 and 9 were excluded from the analysis. Likewise, we needed to exclude Case 7 because the tumour did not grow but shrank between $TP1$ and $TP2$. Therefore, excluding these three cases, our used sample will be referred to as seven cases.

III. RESULTS

A. Synthetic data

Similar to findings in [15], [24], we observed that different combinations of c_{g0} and D_0 yield same results. The sensitivity analysis, a total of 1285 model evaluations, yielded first-order sensitivity indexes of 0.8571, 0.2761 and 0.0048 for D_0 , c_f and c_{g0} , respectively. Applying the dummy parameter eFAST method to our model, we found c_f and D_0 to be significantly different from zero. These results imply that our model is mostly influenced by the diffusive character of tumour growth and thus we fix parameter c_{g0} for further analyses.

Using $TP1$ and $TP2$ for calibration yielded mean relative errors between true and estimated values of 0.71 and 0.23 for c_f and D_0 , respectively. Using the recovered parameters as input for simulations between $TP3$ and $TP5$ resulted in 4.78±8.26%, 3.55±4.95% and 3.81±6.05% volume error, respectively. The DICE-overlap between true and estimated volumes were 97.78±3.6%, 98.30±2.29% and 98.20±2.74%.

B. Pre-clinical data

1) *Cellular evolution simulations*: The initial total cell number for each sub-population and total cell number are

computed as the sum of the cells over the voxels within the tumour boundaries at $TP1$. Using the optimised parameters given in Tab. I, for each time step, the total cell number for each sub-population is computed and used as input for the consecutive time step. The evolution of the proliferating (blue), hypoxic (green) and necrotic (yellow) for all Cases and time points ($TP2 - 5$) are shown in Fig. 2-a. The red crosses represent the true total cell numbers computed as a sum over the voxels within the true masks used for validation. Missing columns are due to missing data for some cases.

Figure 2-b shows the mean absolute cell error for proliferating (blue), hypoxic (green) and necrotic (yellow) for all cases. The error increased with time, so that predictions for later time points ($TP5$) had higher errors than for earlier time points ($TP3$). Additionally, the higher errors were linked to an overestimation in the number of necrotic and hypoxic cells. Relative errors for total number of cells were 0.76±0.67, 1.04±0.94, 1.65±1.73 and 2.69±2.41 for $TP2$, $TP3$, $TP4$ and $TP5$, respectively (see Fig. 2-c).

2) *3-D growth simulations*: On average for all seven cases using the model resulted in a DSC 60.25±10.60, 53.18±16.29 and 50.72±17.43, for $TP3$, $TP4$ and $TP5$, respectively. At later time points the relative volume estimation error increased from 0.45±0.40 at $TP3$ to 1.23±1.08 at $TP5$.

Figure 3 compares the true and estimated cell distributions for a middle slice of the tumour volume evolution for Case 10. From left to right we show true, estimated and residual cell maps for $TP2$, $TP3$, $TP4$ and $TP5$, respectively. For the true and estimated maps, the colour bar represents the number of cells relative to the voxel cell capacity and hence, ranges from 0 to 1. For the residual maps, computed by subtracting the true from the estimated maps, the colour bar ranges from -1 to 1. Hence, negative and positive values represent a local underestimation and overestimation in the estimated cell number, respectively. The black and red outlines within the difference maps represent the true and estimated tumour margin, respectively. The simulated sizes and directions of tumour growth are similar to the ones seen in the true images, especially for early time points. For $TP5$ areas of overestimation can be generally observed at the periphery of the tumour. For $TP3$ and $TP5$, the true images depict parts of the tumour for which no cellularity quantities could be extracted, presumingly where no signal enhancement was achieved due to the presence of necrosis. In the simulated maps those areas depict a smaller cell number but are not completely empty of cells.

IV. DISCUSSION AND CONCLUSIONS

We have presented a reaction-diffusion model of avascular tumour growth constrained by quantitative DCE-MRI data to predict tumour spatio-temporal growth. We first used synthetic data to evaluate our model and its predictive power. Encouraged by our results on synthetic data, we applied our model to data obtained from DCE-MR images for seven preclinical cases of breast carcinoma. Our results demonstrated the feasibility of using maps of cellularity obtained from DCE-MRI analysis to feed and calibrate a model of tumour growth to obtain subject-specific predictions of tumour evolution.

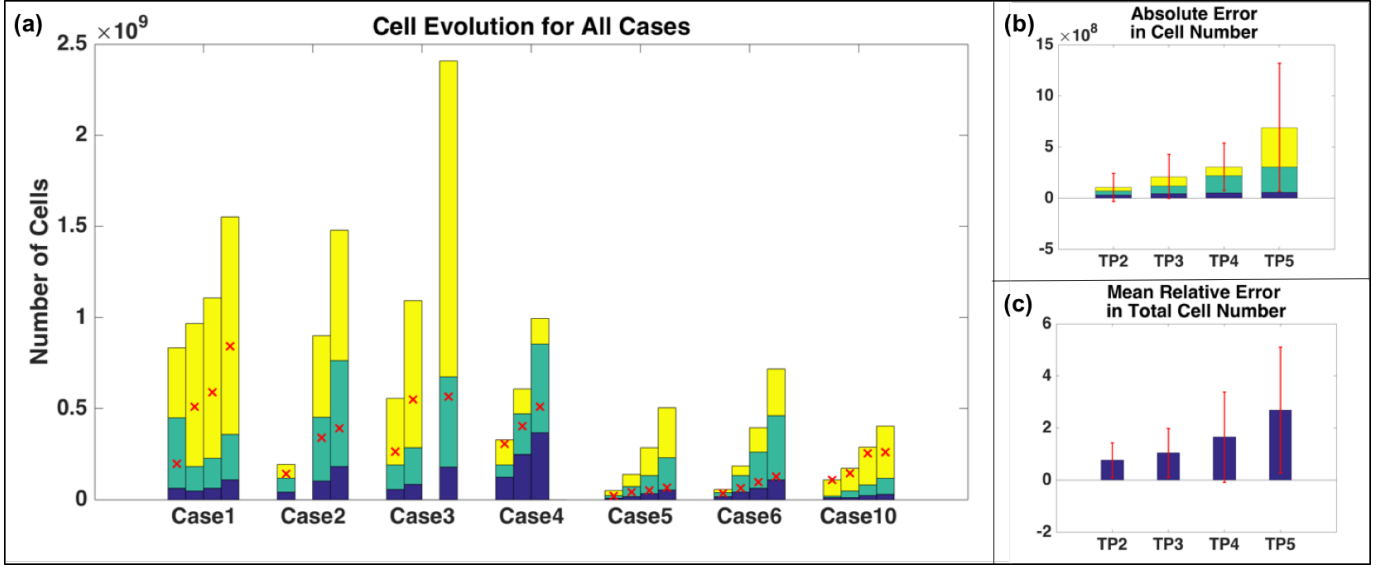


Fig. 2: Simulated tumour cell evolution proliferating (blue), hypoxic (green) and necrotic (yellow) for all cases and time points ($TP2 - 5$) are illustrated as a block-diagram (a). The red crosses represent the true estimated cell number at $TP2$, $TP3$, $TP4$ and $TP5$. Panel (b) and (c) show the mean absolute cell error for proliferating (blue), hypoxic (green) and necrotic (yellow) and the relative error for the total cell number for all cases, respectively.

The results on our synthetic experiments demonstrate that fixing c_{g0} allowed us to accurately predict future tumour growth, manifested in small volume errors and large Dice values, as compared to other studies in the field. For instance, in [12] Diffusion Weighted-MR images were used to constrain a reaction-diffusion model of glioma growth. The *in silico* results showed a percent error in tumour volume ranging between 3.1% and 36.4% and 0.8% and 8.8% when using two and three time points for calibration, respectively. Similarly, in [15] the authors assessed their estimation results based on delineation variability values found their results to be less than a variability value of $0.2mm^2$, which for their tumour translates in a volume error estimation of less than 10%.

The higher cellular prediction and relative volume errors observed at later time points may be due to four reasons. Firstly, the period between the images used for calibration was one day ($TP1$ until $TP2$), so that using the optimised parameters for simulation from $TP2$ onwards might only allow us to predict the volume of the tumour for the same period, i.e. up until $TP3$ (day 3). Secondly, for later time points we expect the tumour to have undergone angiogenesis. Our model, however, does not include angiogenesis, and as such only simulates avascular tumour growth. Thirdly, the largest discrepancy observed in Fig. 2 is linked to the necrotic cell estimation which can be linked to the fact that apoptosis (cell natural death) was not included in our model. To minimise the relative volume error at later time points, we need to investigate whether using $TP1$ and $TP3$ or, as suggested by [12], using three time points to calibrate the model would result in better estimations for $TP4$ and $TP5$. Finally, the fact that no noise has been added to the synthetic data during analysis can also be a potential source of error when dealing with real data and will be explored in a future study.

Our results in Fig. 2 demonstrate that our model performs better for some cases (e.g. Cases 1 and 10) than

others (Case 5 and 6), showing that even within a controlled experiment, using the same sort of subjects and cell lines, tumour progression can vary hugely due to subject-specific microenvironmental aspects. This serves as a motivation to further personalise our model by including information from the surrounding of the tumour which could give additional information to drive tumour expansion. For instance, one could use MRI-Elastography to generate a stiffness map, which could serve as a measure of tissue resistance. Here, the tumour growth would proceed along the lines of the least physical resistance [30].

Figure 2 demonstrates that using cellularity maps from two early time points of tumour development we were able to predict within a reasonable error margin the overall number of cells at later time points. Accounting for each sub-population evolution in addition to the overall volume growth is a strength of the current model compared to other works where all cells within the tumour or a given voxel are assumed to be active and divide at the same proliferation rate [7], [12], [25]. Our model has the potential to evaluate how each cell group contributes to tumour evolution. For instance, in our results, the biggest increase can be seen in the number of necrotic cells suggesting that most of our tumour growth is due to the emergence and growth of necrotic rather than to proliferative areas. In addition, the hypoxic cell numbers could be used to aid treatment planning, as hypoxia is known to play an important role in treatment outcome. However, our results demonstrate that even if the model can predict the total cell evolution within a small range of errors (see Case 10 e.g), it is not able to distribute the cells into the three sub-categories correctly, represented especially by an overestimation in the number of hypoxic and necrotic cells and an underestimation in the number of proliferating cells.

To the best of our knowledge, this is the first attempt to quantify the number of proliferative, hypoxic and necrotic cells

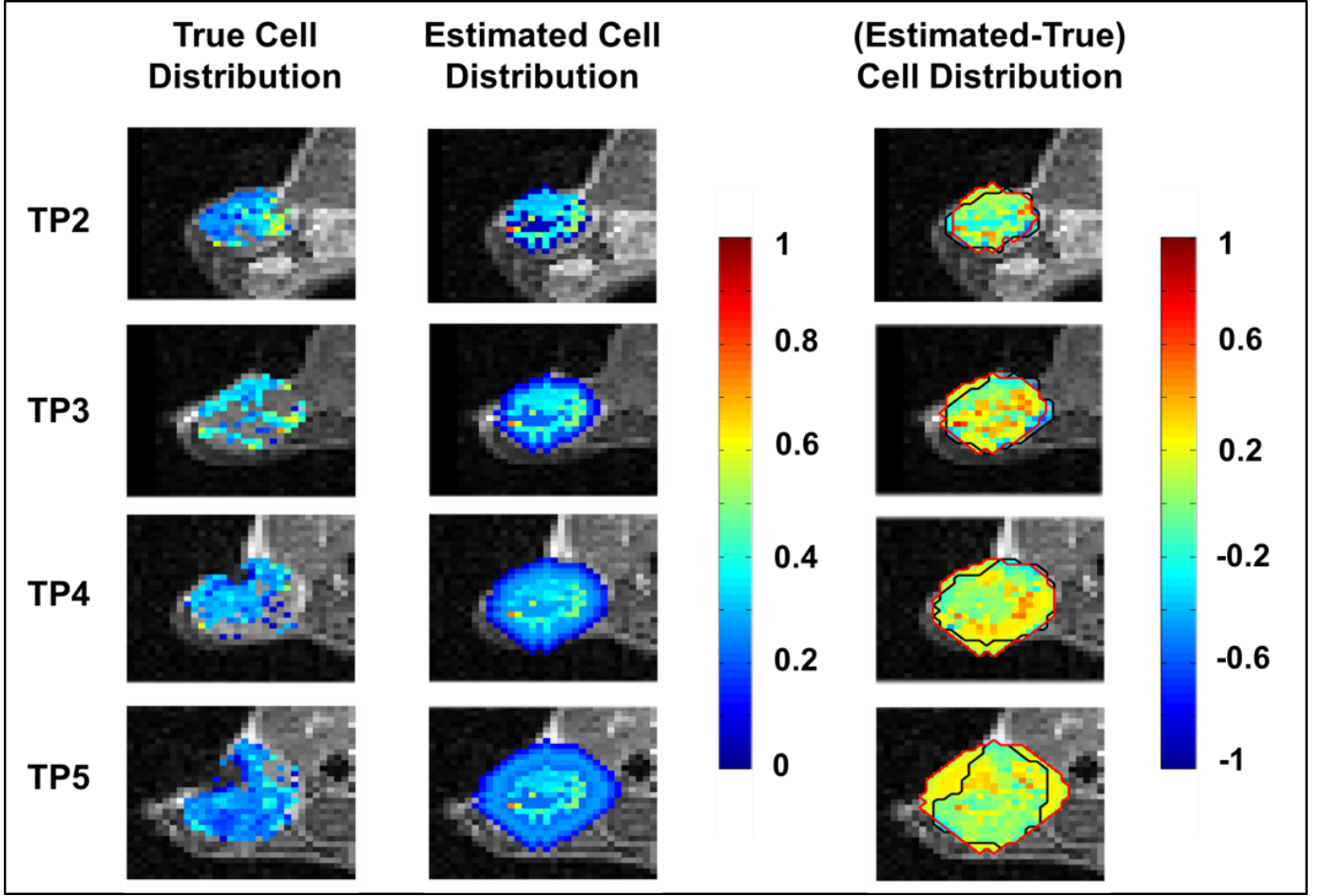


Fig. 3: True and estimated cell distributions for Case 10. The true (left column) and the estimated (middle column) relative cell distributions for an example pre-clinical case are shown for *TP2*, *TP3*, *TP4* and *TP5*. In the right column, for a central slice of the tumour volume, we show the residual maps obtained by subtracting the true maps from the estimated maps. The black and red outlines displayed within the residual images represent the true and estimated tumour delineation, respectively.

using only DCE-MRI maps. Therefore, in the future a comparison of the parameter maps to histo-pathological data should be included in order to validate these maps. Alternatively, because oxygen is the leading nutrient in our model, further tuning of this parameter, e.g. using FMISO-PET scans, could lead to an improvement of the estimation of each cell subpopulation and of the 3D- growth prediction. However, even prior to histo-pathological validation, the comparison between simulated results and the preclinical data shows that the macroscopic growth behaviour of the tumour could be well reproduced. The volume errors could be further reduced by choosing a different diffusion law, which could for instance follow an interstitial pressure gradient instead of the cell gradient implemented herein. Such an interstitial pressure map could be computed using DCE-MRI as proposed by [1].

Even when lysis time is considered, the model fails at predicting some necrotic areas (such as the ones seen in the true maps shown in Fig. 3). This might be linked to our assumption that the tumour centre of mass remains constant over its evolution, so that voxels in the centre of the tumour are assumed to correspond over time. When this is not the case, voxels which were necrotic (and hence empty) at *TP1* but populated in *TP2* might not be the corresponding voxels.

As a result, in the simulated cell maps for *TP2* the voxels will be populated and their cells will continue to proliferate, turn hypoxic or die depending on their nutrient level.

To simplify our model, the simulations were limited to a constant evolution of the nutrient field. For more realistic results, in the future, the nutrient field will evolve following a PDE of the type Eq. 20 and added to the PDE system. This will enable the inclusion of angiogenesis, ultimately allowing for cells in different parts of the tumour to proliferate, turn hypoxic or die independently of their location in the tumour, as nutrient would be provided by small local vessels.

While our model had been built on preclinical data with as many as five time points for imaging tumour growth - a scenario not commonly available in a clinical setting -, our methodology uses only two time points for calibration and one data point for verification, which opens the opportunity to investigate clinical data where therapy is being delivered, using one time point prior to, one during and one post-therapy. To account for therapy, the model needs to be extended accordingly. Such an update could e.g. include the effect of hypoxia on the outcome of therapy. For this, having included hypoxia and nutrient maps in our current model already is a step towards allowing for different therapy outcomes in

different positions and cell groups within the tumour to be modelled. Such an approach could be supported by preclinical data to calibrate and verify the tumour therapy response model prior to clinical application.

ACKNOWLEDGEMENT

We would like to acknowledge funding from the CRUK/EPSRC Oxford Cancer Imaging Centre and from the The Oxford-Bellhouse Graduate Scholarship.

REFERENCES

- [1] M. P. Aryal, T. N. Nagaraja, R. Elmgghribi, K. a. Keenan, S. Panda, G. Cabral, S. L. Brown, and J. R. Ewing. Dynamic Contrast Enhanced MRI Estimate of Tumor Interstitial Fluid Pressure in Solid Brain Tumors. In *Proc. Intl. Soc. Magn. Reson. Med* 23, page 669, 2015.
- [2] M. P. Aryal, T. N. Nagaraja, K. a. Keenan, H. Bagher-Ebadian, S. Panda, S. L. Brown, G. Cabral, J. D. Fenstermacher, and J. R. Ewing. Dynamic contrast enhanced MRI parameters and tumor cellularity in a rat model of cerebral glioma at 7 T. *Magnetic resonance in medicine*, 71(6):2206–14, June 2014.
- [3] N. C. Atuegwu, L. R. Arlinghaus, X. Li, A. B. Chakravarthy, V. G. Abramson, M. E. Sanders, and T. E. Yankeelov. Parameterizing the Logistic Model of Tumor Growth by DW-MRI and DCE-MRI Data to Predict Treatment Response and Changes in Breast Cancer Cellularity during Neoadjuvant Chemotherapy. *Translational Oncology*, 6(3):256–264, June 2013.
- [4] N. C. Atuegwu, J. C. Gore, and T. E. Yankeelov. The integration of quantitative multi-modality imaging data into mathematical models of tumors. *Physics in medicine and biology*, 55:2429–2449, 2010.
- [5] H. M. Byrne and M. Chaplain. Apoptosis and necrosis as distinct cell loss mechanisms in avascular tumour growth. 1:223–235, 1998.
- [6] K. A. Christensen, D. M. Grant, E. M. Schulman, and C. Walling. Optimal determination of relaxation times of fourier transform nuclear magnetic resonance. determination of spin-lattice relaxation times in chemically polarized species. *The Journal of Physical Chemistry*, 78(19):1971–1977, 1974.
- [7] O. Clatz, M. Sermesant, P. Y. Bondiau, H. Delingette, S. K. Warfield, G. Malandain, and N. Ayache. Realistic simulation of the 3-D growth of brain tumors in MR images coupling diffusion with biomechanical deformation. *IEEE Transactions on Medical Imaging*, 24(10):1334–1346, 2005.
- [8] V. Cristini and J. Lowengrub. *Multiscale Modeling of Cancer: An Integrated Experimental and Mathematical Modeling Approach*. Cambridge University Press, 2010.
- [9] O. Fernández-Guinea, A. Andicoechea, L. O. González, S. González-Reyes, A. M. Merino, L. C. Hernández, A. López-Muniz, P. García-Pravia, and F. J. Vizoso. Relationship between morphological features and kinetic patterns of enhancement of the dynamic breast magnetic resonance imaging and clinico-pathological and biological factors in invasive breast cancer. *BMC cancer*, 10:8, 2010.
- [10] M. Heilmann, C. Walczak, J. Vautier, J. L. Dimicoli, C. D. Thomas, M. Lupu, J. Mispelter, and A. Volk. Simultaneous dynamic T1 and T2* measurement for AIF assessment combined with DCE MRI in a mouse tumor model. *Magma (New York, N.Y.)*, 20:193–203, 2007.
- [11] C. Hogue, C. Davatzikos, and G. Biros. An image-driven parameter estimation problem for a reaction-diffusion glioma growth model with mass effects. *Journal of Mathematical Biology*, 56:793–825, 2008.
- [12] D. Hormuth, J. Weis, S. Barnes, M. Miga, E. Rericha, V. Quaranta, and T. Yankeelov. Predicting in vivo glioma growth with the reaction diffusion equation constrained by quantitative magnetic resonance imaging data. *Physical Biology*, 12(4):046006, 2015.
- [13] S. Jbabdi, E. Mandonnet, H. Duffau, L. Capelle, K. R. Swanson, M. Péligrini-Issac, R. Guillevin, and H. Benali. Simulation of anisotropic growth of low-grade gliomas using diffusion tensor imaging. *Magnetic Resonance in Medicine*, 54(3):616–624, Sept. 2005.
- [14] S. Kirkpatrick, C. D. Gelatt, and M. P. Vecchi. Optimization by simulated annealing. *Science*, 220(4598):671–680, 1983.
- [15] E. Konukoglu, O. Clatz, B. H. Menze, M.-A. Weber, B. Stieltjes, E. Mandonnet, H. Delingette, and N. Ayache. Image Guided Personalization of Reaction-Diffusion Type Tumor Growth Models Using Modified Anisotropic Eikonal Equations. *IEEE Transactions on Medical Imaging*, 29(1):77–95, 2010.
- [16] S. Marino, I. Hogue, C. Ray, and D. Kirschner. A methodology for performing global uncertainty and sensitivity analysis in systems biology. *Journal of theoretical biology*, 254 1:178–96, 2008.
- [17] J. M. Murray. Optimal Drug Regimens in Cancer Chemotherapy for Single Drugs that Block Progression through the Cell Cycle. 193:183–193, 1994.
- [18] M. E. Orme and M. A. J. Chaplain. A Mathematical Model of Vascular Tumour Growth and Invasion. *Mathl. Comput. Modelling*, 23(10):43–60, 1996.
- [19] M. R. Orton, J. a. D’Arcy, S. Walker-Samuel, D. J. Hawkes, D. Atkinson, D. J. Collins, and M. O. Leach. Computationally efficient vascular input function models for quantitative kinetic modelling using DCE-MRI. *Physics in medicine and biology*, 53(5):1225–1239, 2008.
- [20] G. J. M. Parker, J. Suckling, S. F. Tanner, A. R. Padhani, P. B. Revell, J. E. Husband, and M. O. Leach. Probing tumor microvasculature by measurement, analysis and display of contrast agent uptake kinetics. *Journal of Magnetic Resonance Imaging*, 7(3):564–574, 1997.
- [21] T. Roque, V. Kersemans, S. Smart, D. Allen, J. Schnabel, and M. Chappell. A dce-mri imaging-based model for simulation of vascular tumour growth. *Conference proceedings: Annual International Conference of the IEEE Engineering in Medicine and Biology Society. IEEE Engineering in Medicine and Biology Society.*, 2016:5949–5952, 8 2016.
- [22] J. A. Sherratt and M. A. J. Chaplain. Mathematical Biology A new mathematical model for avascular tumour growth. 312:291–312, 2001.
- [23] S. P. Sourbron and D. L. Buckley. Classic models for dynamic contrast-enhanced MRI. *NMR in Biomedicine*, 26(February):1004–1027, 2013.
- [24] K. R. Swanson, C. Bridge, J. Murray, and E. C. Alvord. Virtual and real brain tumors: using mathematical modeling to quantify glioma growth and invasion. *Journal of the Neurological Sciences*, 216(1):1–10, Dec. 2003.
- [25] K. R. Swanson, R. C. Rockne, J. Claridge, M. A. Chaplain, E. C. Alvord, and A. R. a. Anderson. Quantifying the role of angiogenesis in malignant progression of gliomas: in silico modeling integrates imaging and histology. *Cancer research*, 71(24):7366–75, Dec. 2011.
- [26] M. D. Szeto, G. Chakraborty, J. Hadley, R. Rockne, M. Muzi, E. C. Alvord, K. a. Krohn, A. M. Spence, and K. R. Swanson. Quantitative metrics of net proliferation and invasion link biological aggressiveness assessed by MRI with hypoxia assessed by FMISO-PET in newly diagnosed glioblastomas. *Cancer research*, 69(10):4502–9, May 2009.
- [27] P. S. Tofts, G. Brix, D. L. Buckley, J. L. Evelhoch, E. Henderson, M. V. Knopp, H. B. Larsson, T.-Y. Lee, N. A. Mayr, G. J. Parker, R. E. Port, J. Taylor, and R. M. Weisskoff. Estimating kinetic parameters from dynamic contrast-enhanced t1-weighted mri of a diffusable tracer: Standardized quantities and symbols. *Journal of Magnetic Resonance Imaging*, 10(3):223–232, 1999.
- [28] P. Tracqui. Biophysical models of tumour growth. *Reports on Progress in Physics*, 72(5):056701, May 2009.
- [29] R. Venkatasubramanian, R. B. Arenas, M. a. Henson, and N. S. Forbes. Mechanistic modelling of dynamic MRI data predicts that tumour heterogeneity decreases therapeutic response. *British journal of cancer*, 103(4):486–497, Aug. 2010.
- [30] R. Wasserman and R. Acharya. A patient-specific in Vivo tumor model. *Mathematical biosciences*, 1996.
- [31] O. Wu, L. Ø stergaard, R. M. Weisskoff, T. Benner, B. R. Rosen, and a. G. Sorensen. Tracer arrival timing-insensitive technique for estimating flow in MR perfusion-weighted imaging using singular value decomposition with a block-circulant deconvolution matrix. *Magnetic Resonance in Medicine*, 50(1):164–74, July 2003.
- [32] T. E. Yankeelov, N. Atuegwu, D. Hormuth, J. A. Weis, S. L. Barnes, M. I. Miga, and E. C. Rericha. Clinically Relevant Modeling of Tumor Growth and Treatment Response. 5(187):1–5, 2013.
- [33] V. L. Yarnykh. Actual flip-angle imaging in the pulsed steady state: A method for rapid three-dimensional mapping of the transmitted radiofrequency field. *Magnetic Resonance in Medicine*, 57(1):192–200, 2007.
- [34] K. L. Zierler. Theoretical Basis of Indicator-Dilution Methods For Measuring Flow and Volume. *Circulation Research*, 10(3):393–407, Mar. 1962.
- [35] L. Ø stergaard, R. M. Weisskoff, D. A. Chesler, C. Gyldensted, and B. R. Rosen. High resolution measurement of cerebral blood flow using intravascular tracer bolus passages. part i: Mathematical approach and statistical analysis. *Magnetic Resonance in Medicine*, 36(5):715–725, 1996.